Low V_p/V_s ratios in the crust and upper mantle beneath the Sea of Okhotsk inferred from teleseismic p_MP, s_MP, and s_MS underside reflections from the Moho

Yingcai Zheng and Thorne Lay
Earth Sciences Department, University of California, Santa Cruz, California, USA

Received 7 March 2005; revised 30 September 2005; accepted 31 October 2005; published 25 January 2006.

[1] Teleseismic ground motion recordings of deep earthquakes often contain clear seismic wave reflections from the free surface above the source (*pP*, *sP*, *sS*), with isolated precursors (p_MP, s_MP, and s_MS) produced by underside reflections from the Moho (the crust-mantle boundary) below the free surface reflection points. The waveforms of the depth phases and their precursors are readily modeled, providing constraints, for steep angles of incidence, on integrated two-way crustal travel times and Moho shear and compressional impedance contrasts above deep earthquake source regions. We model surface reflection waveforms in stacks of three-component, long-period WWSSN and digital broadband seismograms for signals traversing the crust and upper mantle beneath the Sea of Okhotsk, which overlies deep earthquakes in the subducted Kurile slab. The crust beneath most of the Sea of Okhotsk is 19–25 km thick, indicating a submerged continental margin, with minor crustal thinning toward the Kuril back-arc basin, where thin oceanic crust is found. Modeling p_MP and s_MS phases that sample the same subregion provides tight constraints on the V_p/V_s ratio in the crust and uppermost mantle (assuming common density structure and consistent crustal thickness for *P* and *S* waves); the absolute velocities are not constrained by the data. We find unusually low V_p/V_s ratios in the range 1.6–1.7 for the uppermost mantle under the Sea of Okhotsk and comparably low average V_p/V_s ratios for the crust in several regions. The presence of fluids and extensive silica enrichment, possibly involving low-temperature veining, are viable explanations for the anomalous V_p/V_s ratios; this may represent an important process of continentalization taking place landward from the volcanic arc in subduction zones.

Citation: Zheng, Y., and T. Lay (2006), Low V_p/V_s ratios in the crust and upper mantle beneath the Sea of Okhotsk inferred from teleseismic p_MP, s_MP, and s_MS underside reflections from the Moho, *J. Geophys. Res.*, *111*, B01305, doi:10.1029/2005JB003724.

1. Introduction

[2] Determination of seismic properties of the crust is important for understanding crustal formation and evolution, and several decades of effort have been directed at developing first-order models of the crust around the world [e.g., *Christensen and Mooney*, 1995; *Mooney et al.*, 1998]. The key first-order properties of the crust include the average *P* and *S* velocities of the crust, the crustal thickness (defined as the depth to the Moho discontinuity), and the contrasts in *P* and *S* velocities and density across the Moho (important parameters for characterizing the mineralogical contrast between crustal and mantle rocks). The highest resolution of crustal properties is provided by combined multichannel reflection and refraction surveys with controlled sources; until recently this approach has focused on recovering *P* velocity properties of the crust. Use of three-component sensors and teleseismic earthquakes as passive sources has yielded a bounty of results from receiver function and surface wave dispersion analyses, which primarily constrain the shear velocity properties of the crust [e.g., *Levin et al.*, 2002a, 2002b; *Shapiro and Ritzwoller*, 2002]. The Moho discontinuity may involve a complex transitional structure, but is usually relatively pronounced, giving rise to distinct seismic wave reflections, refractions, and conversions. Seismologists have extensively used topside Moho reflection phases (e.g., P_MP and S_MS) and up-going Moho-converted phases (e.g., *Sp*, *Ps*) to infer crustal and Moho properties [e.g., *Jordan and Frazer*, 1975].

[3] For many regions, it is not possible to deploy seismic stations for refraction or receiver function studies, so other approaches have been developed. *Revenaugh and Jordan* [1989] used multiple *ScSH* wave reverberations along extended corridors within the mantle and crust under the western Pacific to invert for laterally averaged crustal thickness and Moho shear velocity impedance contrast. More localized sensitivity can be obtained by analysis of Moho underside reflected phases recorded at teleseismic

0148-0227/06/2005JB003724$09.00

distances as precursors to *PP* or *SS* phases [e.g., *Schwartz and Lay*, 1993; *Carbonell et al.*, 1994; *Katsumata et al.*, 1993; *Zhao et al.*, 1991]. *Schenk et al.* [1989] introduced the modeling of underside reflections from the Moho (p_MP) that arrive before free surface reflection depth phases (*pP*) at teleseismic distances from deep focus earthquakes. These phases involve waves that are steeply incident on the crust in back-arc regions, and they provide perhaps the simplest geometry for measuring integrated (two-wave) travel time through the crust (from the time difference between p_MP and *pP*), and *P* wave impedance contrast at the Moho (from the p_MP/pP amplitude ratio). *Zhang and Lay* [1993] similarly used s_MS precursors to *sS*, enhanced by stacking signals from many stations, to determine the corresponding shear velocity properties of the Moho and crust.

[4] In this study, we extend the analysis of depth phase precursors, simultaneously modeling three different phases, p_MP, s_MP and s_MS (*SH* component) to infer the crustal and the upper mantle structure above a deep focus earthquake zone. The combined data set provides dense spatial sampling and enables direct comparison of average crustal and Moho *P* and *S* velocity structure in the same region. Surprisingly, this has seldom been done using models extracted by compatible procedures. *Zandt et al.* [1994] analyzed broadband data to characterize the southern Altiplano crust using p_MP, s_MS and crustal reverberation phases, finding evidence for anomalous Poisson ratio of the deep crust. Constraints on seismic velocities and Poisson ratio can provide important bounds on the composition of the crust [*Christensen*, 1996].

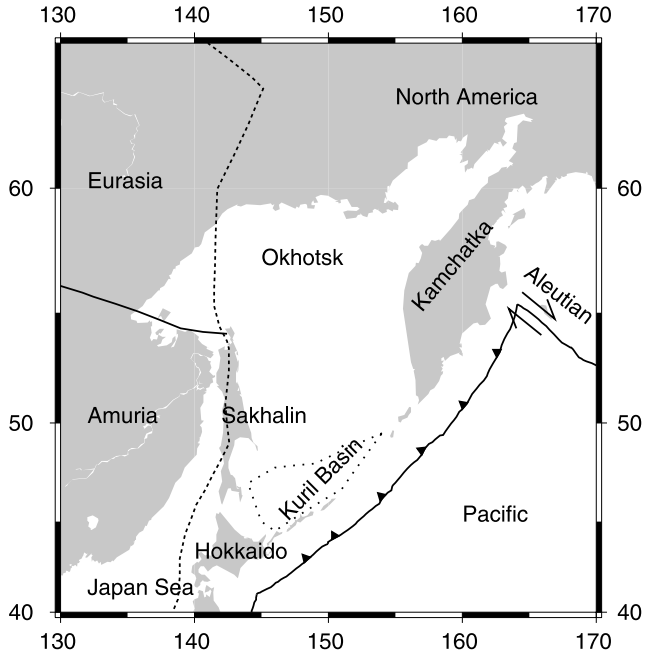

Figure 1. Tectonic map for the Sea of Okhotsk. The Sea of Okhotsk can be divided into an Okhotsk block in the north and the fan-shaped Kuril back-arc basin in the south. Whether the Okhotsk region involves a separate subplate or is part of the North America Plate is unresolved.

2. Tectonic Setting

[5] We use data from deep focus earthquakes in the Kuril subduction zone. The up-going depth phases from these events traverse the upper mantle and crust beneath the Sea of Okhotsk (Figure 1), a submerged terrane on the Eurasian continental margin, before reflecting from the ocean bottom (or free surface) and diving through the mantle to eventually be recorded at teleseismic distances around the world. One unusual attribute of the Sea of Okhotsk is that the regional crust is much thicker than oceanic crust, which helps to isolate depth phase precursors, allowing us to study them with high confidence using both broadband and long-period data.

[6] The tectonic history of the Sea of Okhotsk (Figure 1) is fairly complex, and the nature of the regional crust requires consideration in the context of evolution of the northwestern Pacific margin. The major plate boundaries are well defined. In the northeast, along the western portion of the Aleutian arc, dextral strike-slip motion occurs, intersecting the Kamchatka Peninsula at about 56°N. The Pacific plate subducts northwestward along southern Kamchatka and the Kuril island arc, which extends down to Hokkaido. A right lateral N-S trending fault system is found in Sakhalin and Hokkaido; the formation of this shear zone is thought to be associated with cessation of earlier subduction and reorganization of convergence in the late Cretaceous or Paleogene [*Kimura et al.*, 1983]. This shear zone is thought to be the plate boundary between the North American plate (or a separate Okhotsk plate) and the proposed Amurian plate to the south [*Zonenshain and Savostin*, 1981], the existence of which has been further supported by regional tectonics and earthquake slip vectors [*Wei and Seno*, 1995] and a recent GPS study [*Takahashi et al.*, 1999].

[7] The possibility that the northern Okhotsk block migrated from the south as part of the Kula plate has been considered [*Kimura and Tamaki*, 1986], but is somewhat in question due to the continental nature of the terrane [*Gnibidenko and Svarichevsky*, 1984]. K-Ar isotope age dating of dredged igneous samples indicates that the basement was formed no later than the Cretaceous [*Gnibidenko and Khvedchuk*, 1982]. As for the tectonic identity of the Okhotsk block, there has been no consensus on whether it involves an independent plate [*Cook et al.*, 1986; *Riegel et al.*, 1993] or it is in fact part of the North American Plate [*Chapman and Solomon*, 1976; *DeMets*, 1992; *Seno et al.*, 1996].

[8] Tectonically, the Kurile back-arc basin is bounded on the northern and southern margins by normal faults and the crust is typically thin oceanic back-arc structure [*Gnibidenko and Svarichevsky*, 1984]. The basin has a water depth exceeding 3300 m and a thick (>4 km) undisturbed sedimentary section overlying a rough basement. The opening history of the basin is of importance for the tectonic evolution of the northwest Pacific since the late Cretaceous. Generally, it is thought to have opened in the Miocene [*Ikeda et al.*, 2000; *Maeda*, 1990] and clearly no earlier than the Late Cretaceous [*Gnibidenko et al.*, 1995]. The formation of the Kuril back-arc basin can be explained by the extrusion tectonics model, which accounts for the back-arc spreading as a far-field effect of the India-Eurasia collision in the Eocene [*Worrall et al.*, 1996].

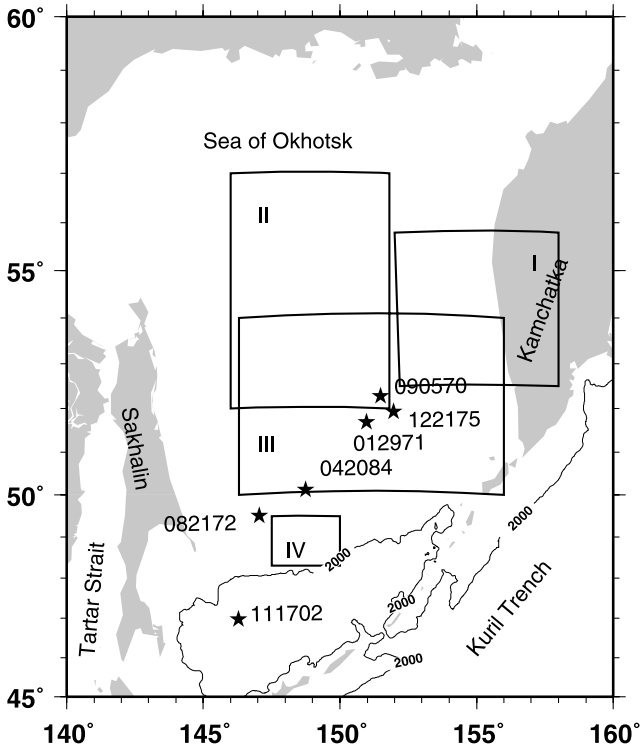

Figure 2. Event locations (stars) in this study along with the 2 km depth isobath contour which delineates the boundary of the Kuril back-arc basin. Numbers beside the stars represent the dates of the events (mmddyy). I–IV designate the region codes for east, north, central, and south Okhotsk.

[9] Our purpose is to add to the seismological characterization of the crust under the Sea of Okhotsk, as this may help in understanding evolution of the regional continental structure.

3. Data and Methods

[10] We analyze digitized three-component WWSSN long-period data from five deep events that occurred in the 1970s and 1980s (Figure 2), as well as broadband data from one recent event (Table 1). There is a paucity of deep earthquakes ($m_b > 6$) in the region since the deployment of extensive digital networks. The need for complete separation of depth phases (Figure 3a) from the down-going (direct *P* and *S*) phases limits our approach to deep focus earthquakes and associated overlying mantle regions. In individual seismograms, we observe clear surface reflected depth phases, *pP*, *sP* and *sS*, preceded by small, but well-isolated Moho underside reflected phases, p_MP, s_MP and s_MS, (Figure 3b). The precursors arrive in time windows that are usually free of other arrivals in our distance range of 35°–90°, but *PP*, *PcP*, *SS* and *ScS* phases must be avoided at some ranges (Figure 3c) [*Zhang and Lay*, 1993]. Receiver coda excited by *pP* tends to increase the noise level for *sP* phases, but for the deepest events, or at azimuths where *pP* is relatively weak, *sP* can be a clear phase with a low noise precursory interval. The arrival time differences and the relative amplitude ratios between the precursors and the surface reflections provide constraints on the coupled parameters of crustal thickness and average crustal velocities and the Moho impedance contrasts through waveform modeling.

[11] To enhance the signal-to-noise ratio for the small precursors from a given event, we align waveforms that have nearby (within 50–100 km) reflection points on *pP* (*sP* or *sS*) and linearly stack them. This procedure is in accord with the intrinsic lateral averaging over each phase's Fresnel zone (the spatial extent contributing to the finite frequency reflections); it reduces scattering and incoherent noise effects, providing stable waveforms for modeling. To eliminate the effects caused by inconsistent gain factors at stations and small source radiation pattern variations, the waveforms are amplitude normalized with respect to a common cycle of *pP* (*sP* or *sS*) prior to stacking. Our analysis involves the relative amplitudes of the precursors and the surface reflections, and is not affected by their absolute values. We only model stacked waveforms from stable portions of the radiation pattern, which limits the sampling provided by any one event.

[12] For the vertical component seismogram analysis (p_MP and *pP*, or s_MP and *sP*), the epicentral distances are carefully selected to avoid interference with energy from *PcP* and *PP* (Figure 3c). The waves radiated from the deep sources can be approximated as plane waves incident beneath the source-side crust. To simplify the computation, we use the Thompson-Haskell propagator matrix method [*Haskell*, 1953, 1960] to calculate the response for a plane wave (single ray parameter) excitation. From the signal processing perspective, the final synthetic waveform $W(t)$ can be written as a series of convolutions in the time domain:

$$W(t) = [S(t)*C_2(t)]*Q(t)*C_1(t).$$

Table 1. Earthquake Parameters Used in the Study[a]

Event	Date	Time, UT	Latitude, °N	Longitude, °E	Depth, km	m_b/M_w	Strike, deg	Dip, deg	Rake, deg
				WWSSN Long Period					
1	5 Sep 1970	0752:27.2	52.28	151.49	582	5.7	3	72	−90
2	29 Jan 1971	2158:03.2	51.69	150.97	544	6.0	34	72	−110
3	21 Aug 1972	0623:48.9	49.51	147.04	578	5.9	15	17	47
4	21 Dec 1975	1054:17.2	51.93	151.97	546	6.0	42	74	−94
5	20 Apr 1984	0631:10.6	50.03	148.76	589	5.9	257	16	−74
				Digital Broadband					
6	17 Nov 2002	0453:53.54	47.82	146.21	459	7.3	324	3	45

[a]For the events recorded by WWSSN the parameters are taken from the ISC catalog, and the magnitude is m_b. Parameters of event 6 are from the USGS/NEIC catalog; the magnitude is M_W.

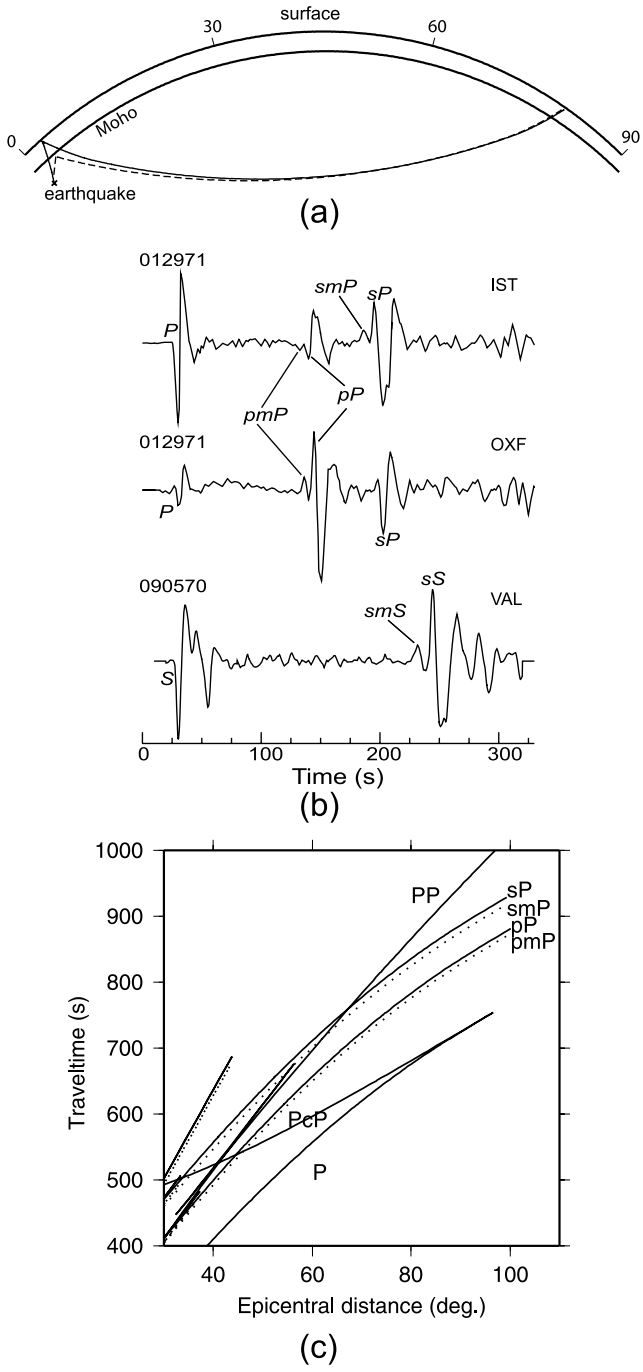

Figure 3. (a) Schematic geometry of ray paths for surface reflection phases *pP*, *sP*, or *sS* (solid line) along with their correspondent Moho underside reflected phases p_MP, s_MP, or s_MS (dashed line). (b) Sample seismograms showing the well-isolated Moho precursors; epicentral distances for stations IST, OXF, and VAL are 74.8°, 79.2°, and 75.5°, respectively. (c) Travel time curves of different phases for a 500 km depth source in model PREM.

Here $S(t)$ is the effective source time function, which is estimated by stacking the direct *P* (or *SH*) arrivals within appropriate epicentral distances (i.e., avoiding upper mantle triplications and core diffractions). $C_2(t)$ is the receiver-side crustal response, which has only a minor effect on the precursors and the first half cycle of the surface reflections (an averaged version of this term is contained in the empirically stacked direct phases). $Q(t)$ is a Futterman differential attenuation operator [*Futterman*, 1962] included to account for the extra attenuation experienced by the surface reflections and the Moho precursors relative to the direct arrivals due to their additional upper mantle transits. $Q(t)$ is chosen to broaden the synthetic *pP* (*sP* or *sS*) pulse to match the observed data. We assume the same differential t^* is valid for the precursor, though a slight over broadening and amplitude decrease of the synthetic pulse could result. This is deemed negligible given the much longer path in the upper mantle shared by precursor and depth phase alike. The $Q(t)$ filter also allows for any pulse width effects of varying source time function between down-going and up-going paths. $C_1(t)$ represents the source-side crustal response. Here, we adopt a simple two-layered model involving a crust (and water layer for *pP* and *sP* modeling) overlying a half-space mantle, so the response effectively involves a precursor caused by underside reflection from the Moho, surface reflections (including a water surface reflection), and all multiples in the crust and water layer. This response provides the flexibility to match the data.

[13] When processing the broadband data, we use a source deconvolution approach [*Langston*, 1979, 2001] to remove the source complexities. We first remove the station instrument responses, stack the direct *P* (or *SH*) arrivals at nearby stations to obtain the effective source time functions for p_MP and s_MP (or s_MS), and then deconvolve the effective source time functions from vertical- (or tangential-) component seismograms using the water level deconvolution method. The water level is determined by trial-and-error methods such that the noise before the direct pulse is minimized. A Gaussian filter, $\exp(-\omega^2/4\alpha^2)$, is applied to exclude high-frequency artifacts resulting from the deconvolution. The deconvolved traces can then be modeled using an attenuated impulse response input into the near-source crustal structure.

[14] Several assumptions are made in our modeling of the bouncepoint structure: (1) we parameterize the crustal properties with linear velocity and density gradients below a thin sedimentary layer since our data cannot resolve and are not very sensitive to internal crustal layering; (2) the sub-Moho density is fixed at ρ_m = 3380 kg/m^3; (3) the modeled density change $\Delta\rho$ across the Moho is scaled in proportion to the *P* wave velocity change ΔV_p according to *Birch*'s [1961] law: $\Delta\rho = 0.3\ \Delta Vp$ in SI units. Generally, there are seven free parameters, crustal thickness (*Th*) and *P* and *S* wave velocities (Vp_m and Vs_m) in the uppermost mantle, *P* and *S* wave velocities (Vp_0, Vp_1, Vs_0, Vs_1) at the top and base of the crust. In order to fit the waveforms, we have to prescribe complete velocity models for the crust and uppermost mantle. Our data place direct constraints only on two-way travel times through the crust for *P* and *S*, and on jumps in *P* and *S* velocity at the Moho (for the assumed density systematics). Given more free parameters than our data can directly constrain we employ a Monte Carlo approach to find suites of modes that satisfy various measures of fit to the observed waveform stacks. In exploring the model space, Vp_m is allowed to vary between 7.1 and 8.2 km/s and Vp_m/Vs_m is varied in the range 1.6–1.8. We further specify the average crustal *P* wave velocity to

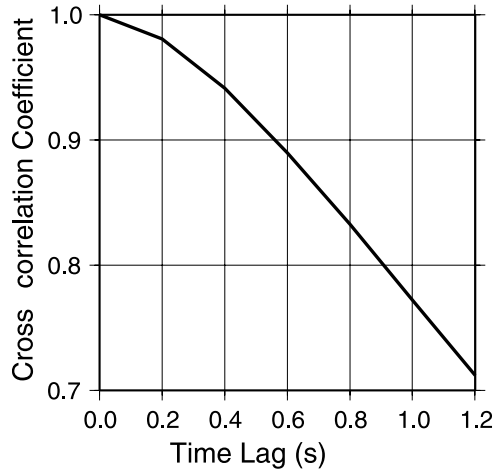

Figure 4. Variation of the autocorrelation coefficient as a function of the time lag for the p_MP wavelet of event 012971pP(A1). Because the input P source time function is similar to the p_MP pulse shape, the autocorrelation will behave like the cross correlation of p_MP with a synthetic.

range from $\overline{V}p \sim 5.8 - 6.4$ km/s and the average crustal shear wave velocity is scaled by $\overline{V}p/\overline{V}s \sim 1.6 - 1.8$. The absolute velocities of the successful models are not resolved (for example, crustal thickness and average crustal velocities trade off), but the data do provide resolution of two model attributes, V_P/V_S ratio of the crust (controlled by relative precursor/depth phase times) and V_P/V_S of the uppermost mantle (controlled by relative precursor/depth phase amplitudes).

[15] Preferred models are selected by two measures: cross-correlation coefficient and the difference of the maximum amplitudes of the precursors in synthetic seismograms versus those in the data. The cross-correlation coefficient alone is sometimes inadequate since it is primarily sensitive to the relative time lag between the observed waveforms and the synthetics, and lacks precise sensitivity to the amplitude of small precursor phases. The threshold for acceptable cross-correlation coefficient for satisfactory fits is chosen based on experimental justification. Figure 4 indicates that the tolerance of the travel time mismatch is prescribed by the cross-correlation threshold. For the amplitude fitting, we compare the maximum amplitudes of the well-isolated Moho underside reflected precursors (e.g., p_MP, s_MP and s_MS) with the synthetics because after stacking the observed waveforms are smooth and accurately modeled. Correlation measures control our differential travel times and amplitude measures then control impedance estimates.

4. Results

[16] On the basis of the geometry of the reflection points, we divide our sampling of the Sea of Okhotsk into four subregions (Figure 2).

4.1. Eastern Sea of Okhotsk

[17] Both p_MP and s_MS data are available in this area, but s_MP phases do not sample this far from the sources (Figure 5). Event 012971 displays 2 distinct types of

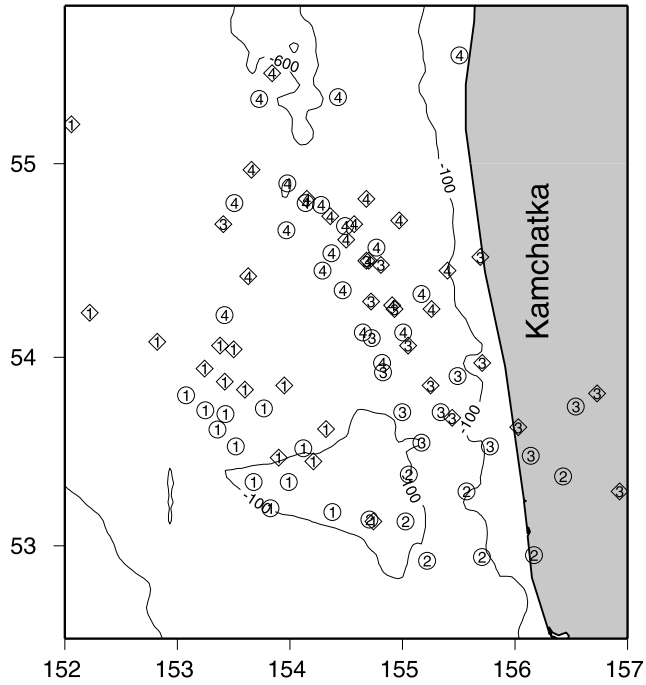

Figure 5. Reflection point distribution in the eastern Sea of Okhotsk region (region I of Figure 2). Each earthquake is associated with a number ("3" for 122175 and "4" for 090570), except event 012971, which has two numbers: "1" (subgroup 012971pP(A1)) and "2" (subgroup 012971pP(A2)). The circles are p_MP bounce points, and the diamonds are s_MS bounce points.

p_MP + pP waveforms (Figure 6), so we subdivide it into a western group, 012971pP(A1), with large p_MP/pP amplitude ratio, and an eastern group, 012971pP(A2), with smaller p_MP/pP ratio. The systematic variation in waveforms between these two groups indicates that the effective spatial extent controlling the reflections is on the

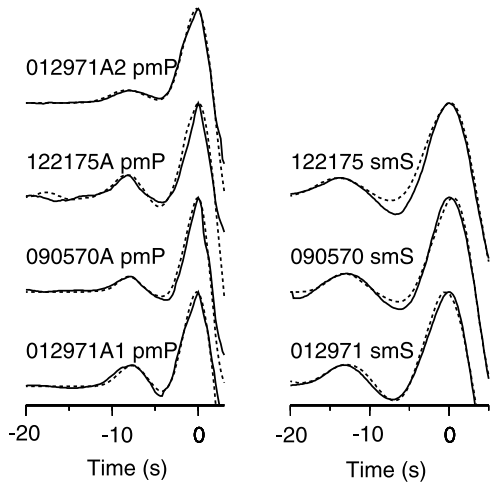

Figure 6. Comparison between synthetics (dashed lines) and data (solid lines) for phases reflecting below the eastern Sea of Okhotsk. These comparisons reflect the quality of fit of various satisfactory models retrieved from the Monte Carlo method.

Table 2. Summary of the Modeling Results[a]

Event	Vs_0, km/s	Vs_1, km/s	Vs_m, km/s	V_{po}, km/s	V_{p1}, km/s	V_{pm}, km/s	Th, km	ΔZ_P, %	ΔZ_{SH}, %
Region I, Eastern Sea of Okhotsk									
012971*pP*(A1) 012971*sS*(A)	3.4 ± 0.1	3.7 ± 0.2	4.8 ± 0.1	5.8 ± 0.2	6.1 ± 0.2	7.7 ± 0.3	21.3 ± 0.9	39 ± 2	41 ± 2
090570*pP*(A) 090570*sS*(A)	3.5 ± 0.2	3.9 ± 0.2	4.7 ± 0.2	6.0 ± 0.3	6.4 ± 0.2	7.6 ± 0.3	24.0 ± 0.8	29 ± 2	31 ± 3
122175*pP*(A) 122175*sS*(A)	3.4 ± 0.1	3.8 ± 0.2	4.7 ± 0.1	5.8 ± 0.2	6.3 ± 0.2	7.8 ± 0.3	25.0 ± 0.8	35 ± 3	35 ± 3
012971*pP*(A2)		···	4.9 ± 0.0	5.8	7.0 ± 0.0	7.3	26 ± 1	18 ± 0	···
Region II, Northern Sea of Okhotsk									
122175*pP*(B) 012971*sP*(B)	3.4 ± 0.1	3.7 ± 0.2	4.6 ± 0.2	5.8 ± 0.2	6.1 ± 0.3	7.5 ± 0.3	20.7 ± 0.8	30 ± 2	31 ± 2
012971*pP*(B) 090570*sS*(B)	3.3 ± 0.1	3.5 ± 0.1	4.6 ± 0.2	5.8 ± 0.2	6.1 ± 0.3	7.6 ± 0.3	22.4 ± 0.8	35 ± 2	41 ± 2
Region III, Central Sea of Okhotsk									
082172*pP*(A) 042084*sS*(A)	3.6 ± 0.2	3.9 ± 0.1	4.6 ± 0.1	5.8 ± 0.2	6.4 ± 0.2	7.8 ± 0.2	19.4 ± 0.5	32 ± 2	28 ± 3
Region IV, Kuril Back-Arc Basin Edge									
111702*sP*(BK)	3.31	3.69 ± 0.03	4.5	5.8	6.45 ± 0.06	8.0	15.5 ± 0.4	···	34 ± 1
111702*sP*(CI/US)	3.31	3.83 ± 0	4.5	5.8	6.7 ± 0	8.0	21.5 ± 0.5	···	28.2 ± 0
111702*sS*(CI)/*pP*(CI)	3.2 ± 0.2	3.6 ± 0.1	4.7 ± 0.1	5.8 ± 0.2	6.4 ± 0.2	7.8 ± 0.2	17.9 ± 0.6	33 ± 3	39 ± 3

[a]The errors are model variance and the entries with no error bars are fixed a priori.

order of 100 to 150 km, which is about half of the calculated 15 s period Fresnel zone radius of 150 km for corresponding *pP* phases by *Schenk et al.* [1989]. There is observed variability within the groups but this is not spatially systematic and we attribute it to noise effects or structural effects that cannot be modeled with localized one-dimensional models. We believe we can reliably recover lateral variations in average reflector properties over scale lengths of about 150 km with our method. Finer-scale variations in Moho depth or average crustal properties undoubtedly exist, but cannot be resolved reliably with WWSSN station distribution; analysis of broadband array data can resolve more localized variations as shown later. The eastern group samples close to the Kamchatka peninsula, but this is also true for the data for event 122175, which has large p_MP/pP ratio, so the variations are not simply related to crustal thickness or water depth. The p_MP and s_MS reflection points overlap for western and northern portion of this region (Figure 5). Thus it is natural to perform joint waveform modeling for $p_MP + pP$ and $s_MS + sS$ by assuming a common crustal thickness for the *P* and *SH* reflections.

[18] We incorporate a 2-km-thick sediment layer (V_P = 2.5 km/s, V_S = 1.25 km/s, ρ = 2600 kg/m^3) in the shallow crust for this region based on the sedimentary map by *Gnibidenko and Khvedchuk* [1982]. Water depths are 0.5, 0.3, and 0.1 km for groups 012971*pP*(A1), 090570*pP*(A) and 122175*pP*(A), respectively. Because the number of constraints provided by the data is less than the number of model parameters, complete crustal models are not uniquely determined, and we find a range of acceptable structures in the Monte Carlo approach, with the mean properties being listed in Table 2. Misfit thresholds are defined by cross-correlation coefficient of 0.95 and 5% error in the peak amplitudes of p_MP or s_MS, which provides suites of models with very good fits to the waveforms (Figure 6).

[19] The strongest trade-off in the model space is between average crustal velocities and crustal thickness, which are together constrained by the two-way travel times. *Levin et al.* [2002a] obtained crustal velocity models on a profile across Kamchatka around 56°N, with Moho depth estimates of 33–38 km, but this is northeast of our sampled region and the offshore crust may be different in character, so we do not impose a priori constraints on the crustal model. Given the robust measures of the *P* and *S* wave two-wave times intrinsic to our data, we obtain tight constraints on the average V_p/V_s ratio for the crust, with three consistent estimates of 1.68 ± 0.02, 1.68 ± 0.02, and 1.67 ± 0.02 for events 122175, 090570, and 012971, respectively. These low ratios are consistent with laterally uniform felsic composition of the overall crust. Other parameters of the crust are not resolved by our data, but for the simple crustal parameterization used, we obtain suites of models that fit the data with some consistent characteristics. To give a sense for successful models, we computed the mean and variance of parameters for the successful models and list these in Table 2. Note, for example that low V_{P1} values are a common attribute, higher *P* velocities in the deep crust may exist, in a more complicated structure, but the overall V_P/V_S ratio of the crust must be preserved. Increasing average $\overline{V}_P$ of the crust leads to very high $\overline{V}_S$ and large V_{pm} values. The estimated crustal thickness for our successful models increases toward the Kamchatka peninsula (Table 2) but is significantly thinner than the onshore estimates from *Levin et al.* [2002a].

[20] Variation of the Moho impedance contrasts in this area indicates that the seismic properties near the Moho do vary laterally. The precursor amplitude information combines with the relative crustal velocity constraints to give estimates of impedance contrasts at the Moho (Table 2) from which we obtain the V_p/V_s ratio of the uppermost mantle. All of the satisfactory models indicate that the uppermost mantle V_p/V_s ratio is very low, 1.65 ± 0.02, 1.62 ± 0.01, and 1.60 ± 0.01 for events 122175, 090570, and 012971, respectively (Figure 7). The ratio increases somewhat as the reflection region approaches the Kamchatka peninsula. These low values are a surprising result and will be discussed in detail below. The results are very similar if we modify our assumed mantle density to 3100 kg/m^3 or if we modify the velocity-density scaling to use $\Delta\rho = 0.2\ \Delta Vp$.

[21] For the group 012971*pP*(A2), with weak p_MP/pP amplitudes, we do not have corresponding s_MS data, and the *pP* modeling obtains a good fit with higher V_p in the lower crust than in the other models (and a smaller jump at the

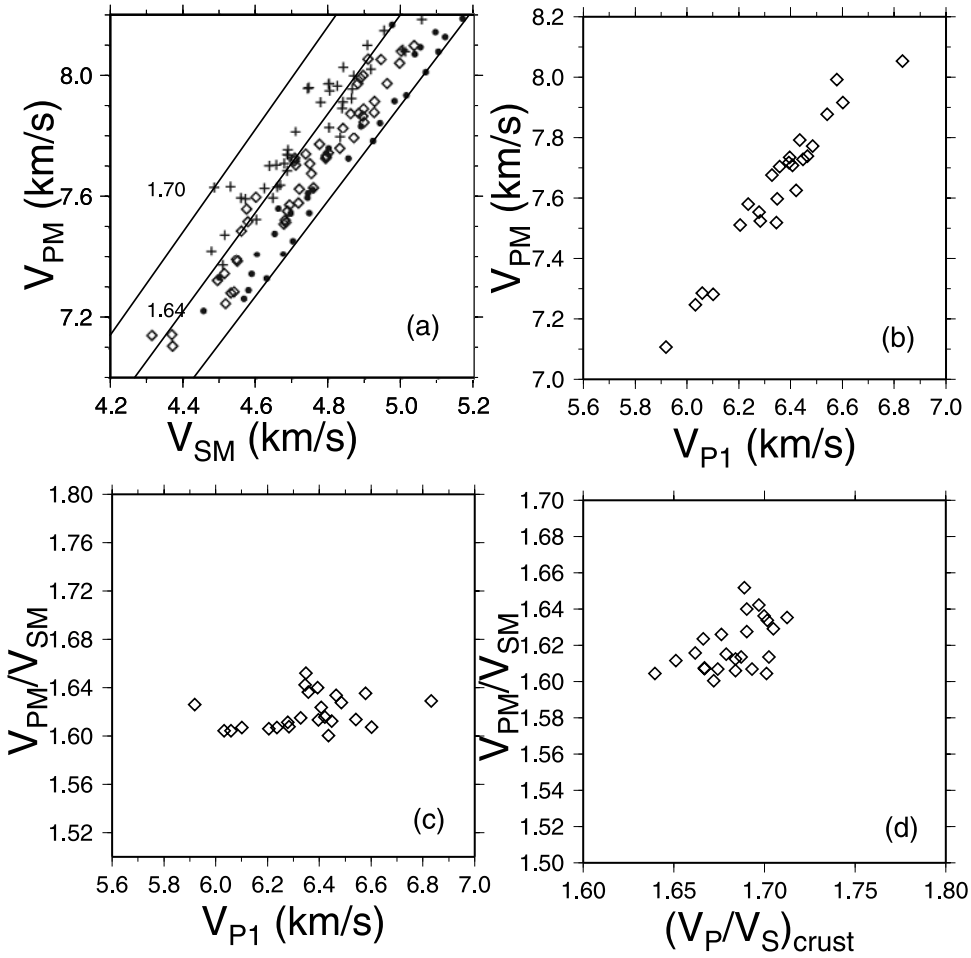

Figure 7. (a) Monte Carlo inversion for the upper mantle V_{pm} and V_{sm} velocities for 012971*pP*(A1) (circles), 090570*pP*(A) (diamonds), and 122175*pP*(A) (pluses). Each symbol indicates a successful model fitting the data to the prescribed tolerances. While absolute velocities are not resolved, the V_{pm}/V_{sm} ratios are well defined for each event by the suites of successful models. (b, c, d) Parameter trade-offs are also displayed. In Figure 7d, $(V_P/V_S)_{\text{crust}} = (V_{p0} + V_{p1})/(V_{s0} + V_{s1})$.

Moho), along with a thicker crust (Table 2). This result is indicative of models that can fit *pP* data or *sSH* data alone; the absolute velocities are not resolved, but when *pP* and *sSH* data are fit simultaneously, the anomalous V_p/V_s ratios of the regional crust and uppermost mantle are immediately apparent. The behavior of the data is made clear if one first fits the *pP* data with a model and then invokes conventional V_p/V_s scaling ratio to predict the *sSH* data. This gives a poor fit, and one requires an incompatible crustal thickness 4–5 km thinner than in the V_p model to fit the *SH* data acceptably. Because the data and modeling are so simple and significant local averaging has been achieved in the stacking, it is difficult to invoke noise or small-scale structural heterogeneity arguments to account for the unusual ratios. Other possible factors such as anisotropy or reflection from dipping Moho are considered below.

4.2. Northern Sea of Okhotsk

[22] This region is sampled by all three types of reflected phases from two events, although the spatial sampling of s_MP is rather isolated (Figure 8). The latter phase has not been previously used for constraining the crustal and Moho properties, so we characterize its sensitivity here. For steep angles of incidence, the s_MP amplitude is only a weak function of V_p at all. To demonstrate this, we consider a two-layered model involving a crust of constant velocities and density overlying a homogeneous half-space mantle. Figure 9 shows that the mantle *P* wave velocity V_{pm} has no influence on s_MP at all while the crustal *P* wave velocity V_{pc} does have some effect on the differential travel time between s_MP and *sP*. The dominant factors affecting s_MP amplitude and relative travel time are the shear wave velocities in the mantle and crust. These results are easily confirmed theoretically by calculating the s_MP reflection coefficient using the appropriate formula of *Aki and Richards* [1980]. We find $|\partial A/\partial\beta_i| \gg |\partial A/\partial\alpha_i|$, where A, α_i, β_i are *S*-to-*P* reflection coefficient of a solid-solid interface, *P* and *S* wave velocities, respectively. The s_MP amplitude thus constrains the shear impedance contrast at the Moho, providing the same information as s_MS if no anisotropy is involved. It is important to note that p_MP behavior is also dependent on the upper mantle shear wave velocity, so we do not have a complete separation of *P* and *S* velocity probes. In Figure 10 we show results for a two-layer model

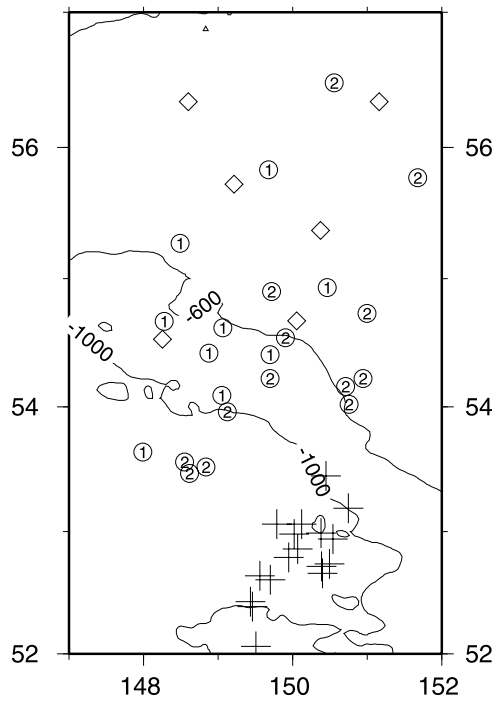

Figure 8. Reflection point distribution in the northern Sea of Okhotsk (region II of Figure 2). Circles are p_MP reflection points of different events, discriminated by the numbers "1" for event 012971 and "2" for event 122175; s_MS (diamonds, event 090570) and s_MP (plusses, event 012971).

demonstrating the sensitivity of p_MP amplitude to mantle V_s. With increasing V_s, the p_MP amplitude drops dramatically.

[23] We perform joint waveform modeling for 012971*pP*(B) and 090570*sS*(B) data stacks and 122175*pP*(B) and 012971*sP*(B) data stacks (Figure 11). In the joint modeling procedure, we include a 0.8 km thick water layer and a 0.5 km thick sediment layer using the same sediment seismic properties as listed before. The waveform fits are again very good for models achieving our thresholds, and trade-offs are similar to those found in modeling the eastern Sea of Okhotsk. Average crustal V_p/V_s ratios from modeling the two pairs of observations (*pP* and *sS* and *pP* and *sP*) are 1.77 ± 0.01 and 1.70 ± 0.02, respectively. The estimated depth of the Moho is ~22 km. The upper mantle velocity structure is similar to that found for region I, involving low V_{pm}/V_{sm} ratios ranging from 1.6 to 1.7 with averages of 1.63 ± 0.02 for both data sets (Figure 12). Table 2 indicates the average models found in each case, with there being some variation in all velocities. This could be the result of the slightly different spatial sampling involved in each data group or the result of different sensitivity to the source wavelet and its frequency content (for *sP* modeling, we use a stacked *P* wavelet with differential attenuation, whereas for *sS* modeling we use a stacked *SH* wavelet with differential attenuation). The noise levels tend to be higher for *sP* arrivals, so the results for these phases are not as reliable as *sS* modeling.

4.3. Central Sea of Okhotsk

[24] This region is sampled by surface reflections for two deep Kurile slab events (Figure 13). The s_MS and p_MP waveforms are modeled jointly (Figure 14) and water depth is set to 1.0 km, with no sedimentary layer being added. In actuality, this region may have a very thin (≤0.5 km) sediment layer; however, modeling results show that such a thin layer has little effect on the synthetic waveforms. The average crustal V_p/V_s is found to be 1.63 ± 0.02 and the crustal thickness is estimated at ~19.5 km (Table 2). The average V_{pm}/V_{sm} ratio is ~1.69 ± 0.02 (Figure 15). The latter estimate could be increased to 1.72 ± 0.02 if we allow different crustal thicknesses (1.0 km difference) for s_MS and p_MP due to the slight offset in their reflection points.

4.4. Southern Sea of Okhotsk

[25] Three-component broadband data from the Berkeley Digital Seismic Network stations (BK), Caltech TERRAScope/TriNET stations (CI), and North American Global Seismic Network stations (US) are used to constrain the crustal structure near the northern margin of the Kuril back-arc basin. These data are from relatively dense distributions of stations and the stacked s_MP waveforms

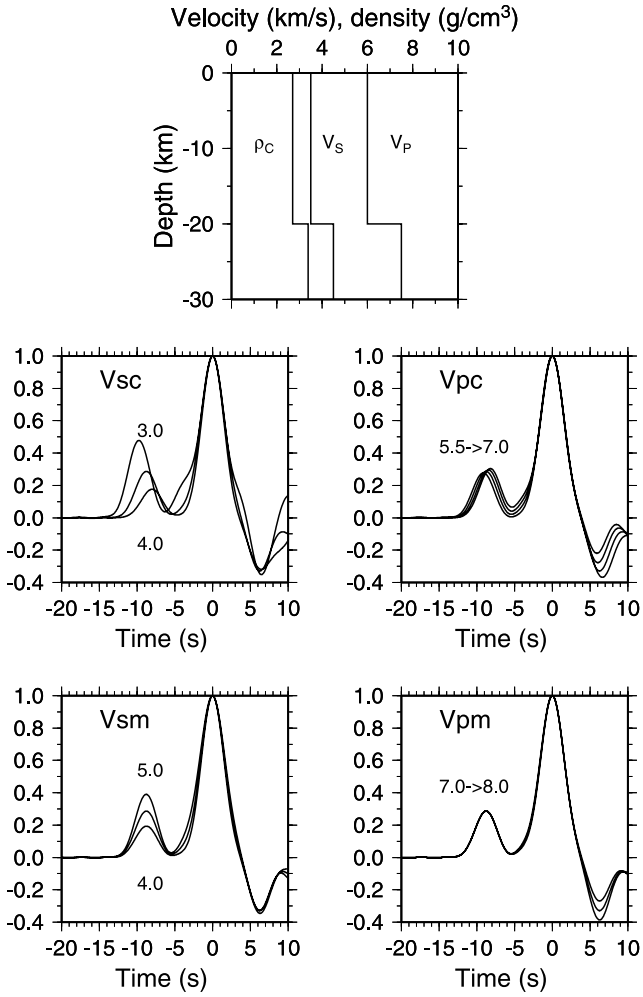

Figure 9. Effects of model variables on s_MP amplitude. We investigate the sensitivity by varying individual parameters over the indicated range while holding the others at the initial values. The ray parameter is 6.0°/s. V_{sc} and V_{pc} are the *S* and *P* velocities in the crust, respectively; V_{sm} and V_{pm} are the *S* and *P* velocities in the mantle.

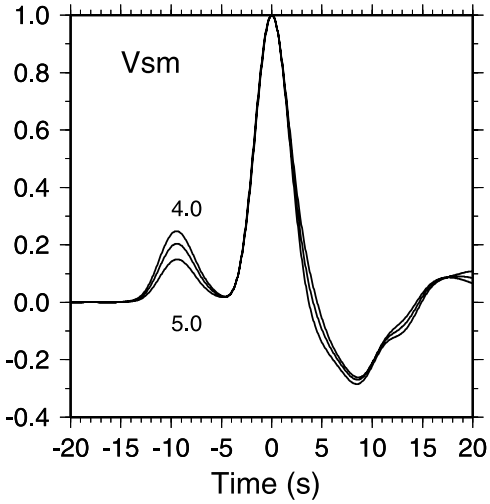

Figure 10. Effect of uppermost mantle shear velocity on the p_MP amplitude for a ray parameter 6.0°/s. The model for this test is same as in Figure 9, except the crustal thickness is 30 km.

indicate systematic variation on relatively small-scale lengths (Figure 16a). Estimates of Moho shear velocity properties are obtained by modeling these phases (Table 2), but there are no *pP* reflections in the same area for simultaneous inversion so we hold the *P* wave velocity to be the same as in model PREM [*Dziewonski and Anderson*, 1981]. The waveform variations are clearly apparent in the data, indicating small effective Fresnel zones for these phases. The s_MS and p_MP reflection points for the CI stations overlap within a zone about 20 km across (Figure 16b). We model these s_MS and p_MP phases simultaneously, obtaining an average mantle V_{pm}/V_{sm} ratio of 1.66 ± 0.03 (Figure 17), while the average crustal V_p/V_s is a high value of 1.79 ± 0.03.

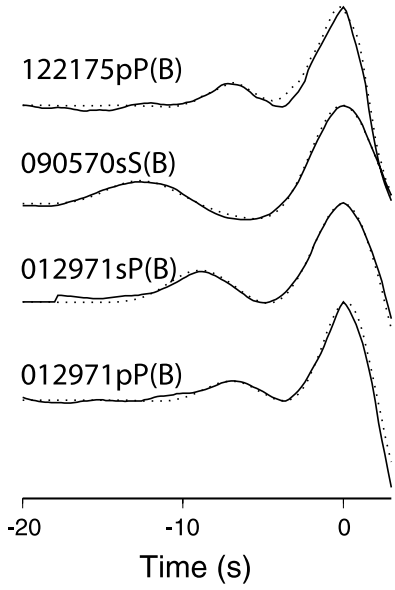

Figure 11. Comparison between synthetics (dashed lines) and data (solid lines) for phases reflecting below the northern Sea of Okhotsk.

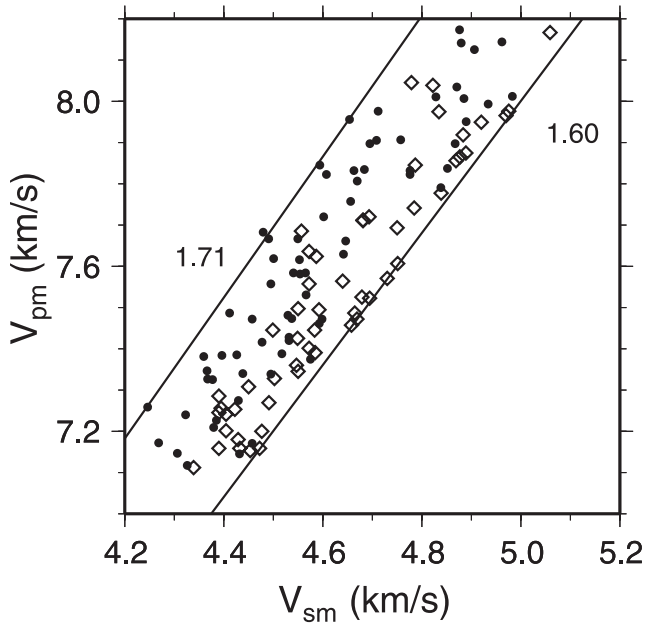

Figure 12. Monte Carlo inversions for V_{pm} and V_{sm} for 122175*pP*(B) and 012971*sP*(B) data stacks (diamonds) and 012971*pP*(B) and 090570*sS*(B) data stacks (circles) for the northern Sea of Okhotsk.

The crustal thickness is ~18 km which suggests that the Sea of Okhotsk crust thins slightly toward the Kuril back-arc basin from the north and east.

5. Discussion

[26] The Sea of Okhotsk is an exotic terrane that does not have a clear tectonic history defined. The various regions of the Sea of Okhotsk sampled in our study are characterized by intermediate, 19–24 km thick crust, low V_p/V_s ratios in the crust except near the Kurile basin, and anomalous uppermost mantle with V_p/V_s < 1.7 across the region. According to *Christensen and Mooney* [1995], thin continental crust may overlay a weak and thin lithosphere and the crust is likely to be thickened by subcrustal flow. However, it is unclear whether the Sea of Okhotsk crust is

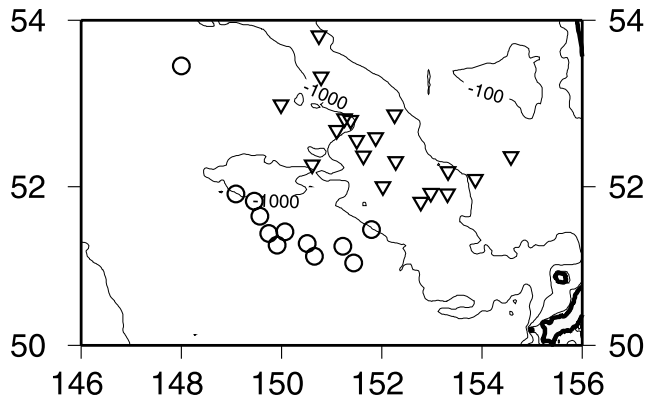

Figure 13. Central Sea of Okhotsk reflection points for p_MP (circles) of event 082172 and s_MS (triangles) of event 042084.

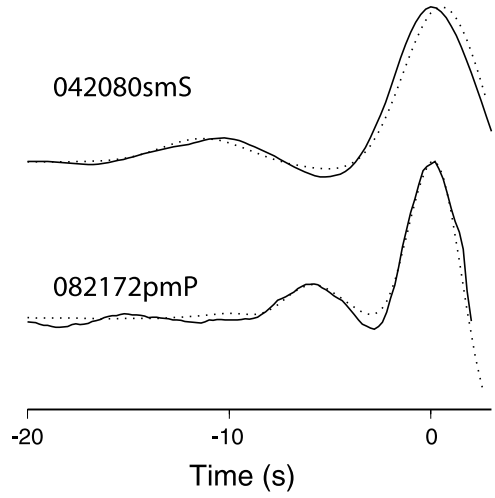

Figure 14. Comparison between synthetics (dashed lines) and data (solid lines) for phases reflecting below the central Sea of Okhotsk.

continuing to thicken by deformation or by some process of continentalization and underplating. Our seismic velocity estimates may provide some guidance on this issue.

[27] In the preliminary reference Earth model (PREM) [*Dziewonski and Anderson*, 1981] the average shear and compressional impedance contrasts at the Moho are 29.2% and 32.6%, respectively. *Lerner-Lam and Jordan* [1987] used Rayleigh waves to build models EU2 and PA2 for northern Eurasia and the Pacific Ocean. The shear and compressional impedance contrasts at the Moho are 26% and 28.8% in EU2 and 36.8% and 38.4% in PA2, respectively. These results suggest that oceanic regions have higher impedance contrasts than continental regions. Note that the compressional impedance contrasts are larger than the shear impedance contrasts in these models. This is because the V_p/V_s ratio in the uppermost mantle (~1.81 in PREM) is larger than in the lower crust (~1.74 in PREM).

[28] In the Sea of Okhotsk region, V_p/V_s ratios less than 1.7 for the uppermost mantle are found throughout our study area, for both WWSSN and broadband data. Results from the eastern Sea of Okhotsk based on WWSSN data and the southern Sea of Okhotsk based on the broadband data are best resolved because of the their dense geographic sampling of the bounce points and overlapping reflection zones that make the joint inversion accurate. However, less reliable results from other regions generally corroborate the most reliable ones.

[29] The depth extent of the anomalous V_P/V_S ratio region in the uppermost mantle is not resolved by the data, but we note that there are no clear additional precursors that would suggest a discrete layer. We estimate that the depth extent is on the order of $\lambda/4 \sim 30$ km, given the impulsive long-period reflection, but a thinner zone could be involved. Constraining the depth extent on the basis of *pP*, *sP*, and *sS*

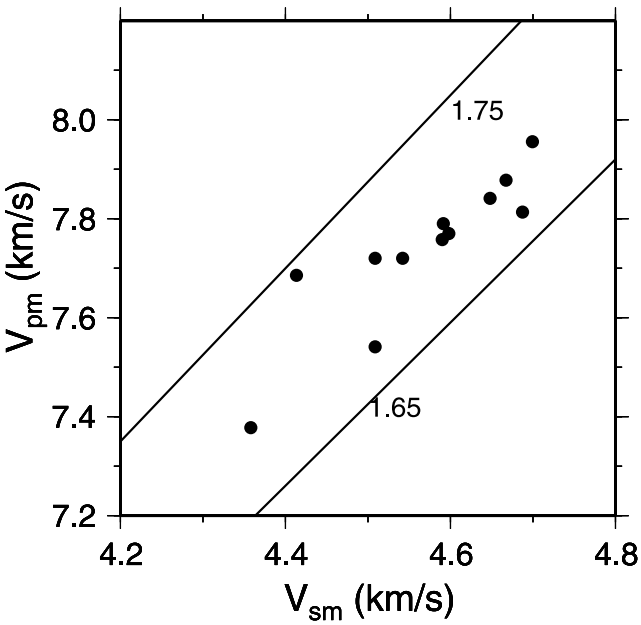

Figure 15. Monte Carlo inversion for upper mantle V_{pm} and V_{sm} for 082172*pP*(A) and 042084*sS*(A), which sample the central Sea of Okhotsk.

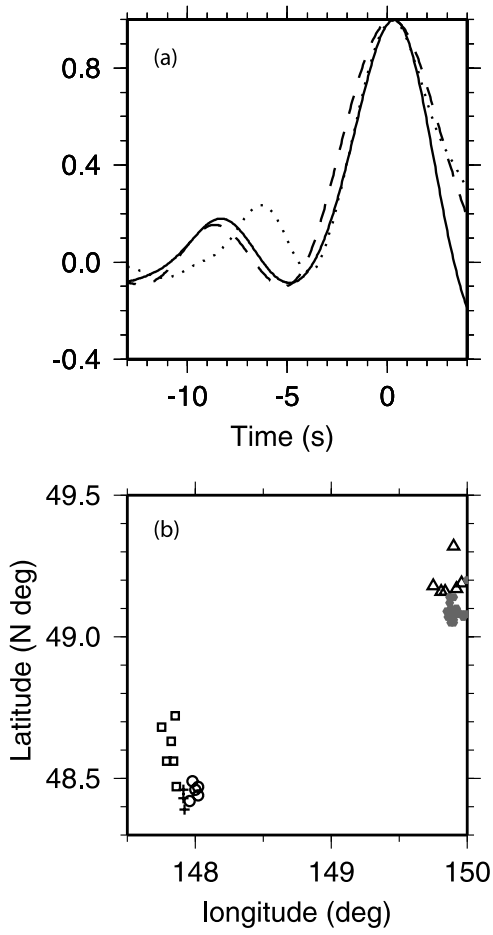

Figure 16. (a) Stacked source-deconvolved s_MP waveforms of network BK (Berkeley Digital Seismic Network stations; dotted lines), CI (Caltech Terrascope/TriNet stations; dashed lines) and US (North American GSN stations; solid lines). (b) s_MP reflection points (BK (circles), CI (pluses), and US (squares)) and CI p_MP (triangles) and s_MS (shaded circles) reflection points.

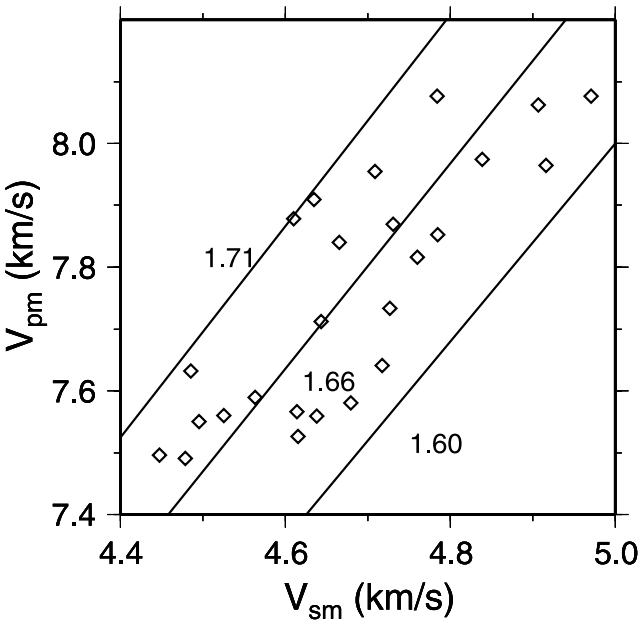

Figure 17. Monte Carlo inversion of mantle V_{pm} and V_{sm} for the southern Sea of Okhotsk.

relative arrival times may be worth attempting, but requires more data than we have available. Our inverted results are for localized one-dimensional models, and failure to account for three dimensional effects could bias the results, although it seems remarkable that this would occur in all four regions for which simultaneous modeling of *pP* and *sS* or *pP* and *sP* was conducted. Nonetheless, wave propagation processes that modify the *pmP*/*pP* or *smS*/*sS* amplitude ratios could be misleading our 1-D interpretations. Focusing or defocusing effects with very small-scale lengths could occur, either along the up-going paths, at the Moho, or at the surface reflection points. Anomalously strong crustal attenuation could affect amplitude ratios as well. However, there is no indication of such effects, and they would have to persist despite stacking and averaging. The long-period data are rather insensitive to attenuation, particularly over short differential paths such as the crustal legs for the depth phases. Another possibility is misinterpretation due to an overly simplified crustal model parameterization. Perhaps complex crustal layering, with thin high- and low-velocity layers can explain the data without overall V_P/V_S anomalies. While the associated model space is infinite, we did explore many forward models with alternate parameterizations. No clear promising direction for reparameterizing the crustal model emerged; in general, the integrated V_P/V_S ratio in the crust remains low despite fine-scale structure being introduced. The long-period waveforms provide little sensitivity to internal crustal structure, but the data are well modeled with our simple crustal parameterization, and no extra complexity is demanded. In some cases, crustal layering corrupts the waveform fit, so very exotic crustal models may be untenable.

[30] Anomalous V_p/V_s ratios are not novel in subduction zones [e.g., *Zandt et al.*, 1994; *Wagner et al.*, 2005]. However, in most cases, low V_p and high V_p/V_s ratios are found, which is usually attributed to either partial melting or mantle serpentinization. Unfortunately, our resolution of absolute velocities is very limited, and independent constraint on crustal or upper mantle properties is not available on localized scale compatible with our data. Additional information is needed in order to investigate the physical and compositional properties of the uppermost mantle in the region. *Fedotov and Slavina* [1968] found decreasing *P* wave velocities in the uppermost mantle from under eastern Kamchatka ($V_p \sim 7.4$) km/s to western Kamchatka ($V_p \sim 7.2–7.3$) km/s. A few seismological studies also favor a low-velocity mantle [*Levshin et al.*, 2001; *Levin et al.*, 2002a, 2002b], and these values are near the low end of the ranges of our successful models (Table 2). However, lacking precise constraints on the absolute values, we will focus on the V_p/V_s ratio.

[31] Partial melting in the mantle will increase the V_p/V_s ratio, while the presence of pore fluids can decrease it [e.g., *Takei*, 2002; *Sato and Ito*, 2002]. This velocity ratio is a function of pore geometry, which is poorly known in the mantle. For isolated pores, assuming needle shape, composite elastic properties (typical mantle peridotite + water) are calculated using the method described by *Watt et al.* [1976] and the results are displayed in Figure 18. Presence of water will lower the V_p/V_s ratio significantly, but meanwhile, it also decreases V_p and V_s dramatically, which is not the case demanded by our results. It is clear that the mantle petrology cannot be sufficiently explained by peridotite whether the hydrous component is present or not. If the low V_p/V_s ratio in the mantle is partly due to the presence of water, this would put bounds on the mantle temperature between 720°C and 900°C. The lower and higher temperatures are to avoid serpentinization [*Ulmer and Trommsdorff*, 1995] and partial melting of the mantle due to presence of a hydrous component [*Winter*, 2001], respectively.

[32] In low-temperature environments distant from silicate melts, SiO_2 could be an important constituent in the uppermost mantle in the form of quartz veins, which may alter the mantle wedge bulk chemistry and mineralogy. The effect of SiO_2 enrichment, or resulting increase in orthopyroxenite, is to lower the V_p/V_s ratio in the uppermost mantle. Fluids released from the slab and subducted sediments can penetrate through the overlying mantle [e.g., *Bebout and Barton*, 1989]. However, our crustal samples are well inland from the arc, so distinct fluid pathways will be needed The rising aqueous SiO_2 fluids, derived from subducted sediment and crust, due to SiO_2 solubility decrease, will precipitate as quartz veins. Quartz veins with orthopyroxene rim in peridotite mantle xenoliths have been recently reported at the subduction zone in Spain [*Arai et al.*, 2003]. The rim will prevent further chemical reaction between SiO_2 and olivine on the vein walls. Such a process will result in a high Mg# (=Mg/(Mg + total Fe) atomic ratio) mantle which has low V_p/V_s ratio. Figure 18 shows the calculated composite material (peridotite + quartz) elastic properties, assuming the silica inclusions are needle shape. The silica inclusion has small effect on absolute velocities but it can decrease V_p/V_s ratio as much as the aqueous fluid can.

[33] A combination of SiO_2 veining and the presence of fluids, may account for the low V_p/V_s ratio. It is important to note that the regions sampled by our data are well landward from the volcanic arc. SiO_2 enrichment by fluids requires low fluid temperatures, and subsolidus conditions. While fluids are commonly invoked to lower melting temperatures

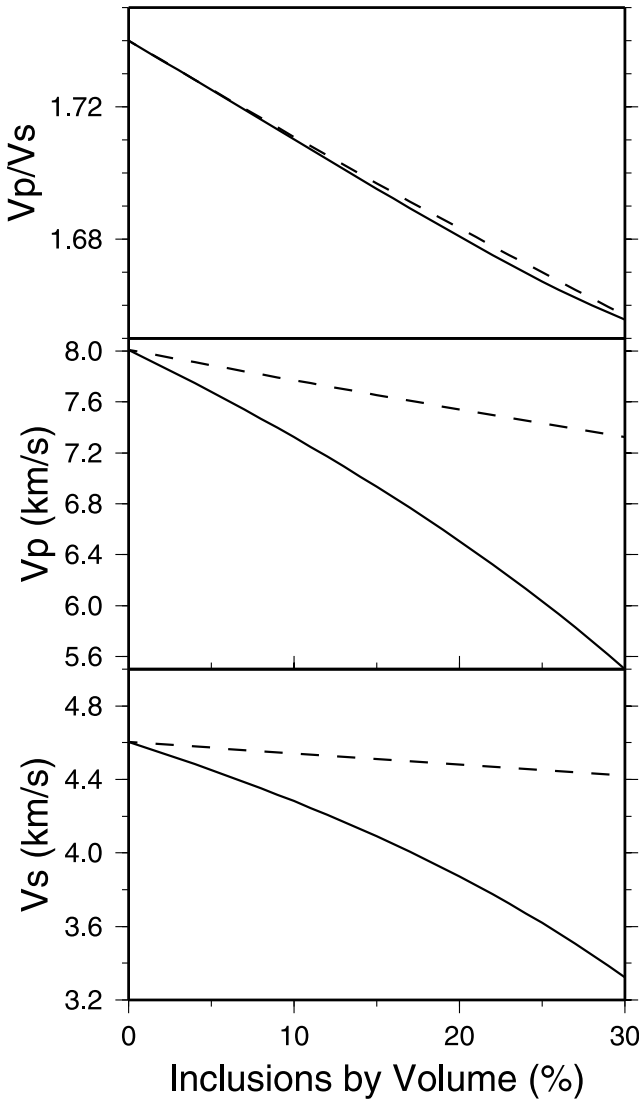

Figure 18. Composite elastic properties for peridotite + water (solid line) and peridotite + quartz (dashed line). *P*, *S* wave velocities and density for peridotite are 8.01 km/s, 4.60 km/s, and 3.38 g/cm^3; for quartz, V_p = 6.09 km/s, V_s = 4.05 km/s, density is 2650 kg/m^3; for water, V_p = 1.5 km/s, V_s = 0 km/s, density is 1000 kg/m^3.

in the wedge, flushing of fluids through the upper mantle inland from the wedge in low-temperature regions could occur progressively over time, building up the fluid content and SiO_2 enrichment. This mechanism could be an unrecognized player in the continentalization of the uppermost mantle and crust landward of the volcanic arc while melting plays a major role. The major challenge to such interpretation is that the amount of quartz and fluids required to affect large volumes of crust and upper mantle is very large, and is not readily accounted for by typical subduction scenarios. Improving constraints on the total volume of rock involved is a next step to take.

6. Conclusions

[34] The crustal and uppermost mantle seismic structures of the Sea of Okhotsk have been investigated by modeling teleseismic Moho underside reflection phases, p_MP, s_MP and s_MS. Anomalously low V_p/V_s ratios (<1.7) in the uppermost mantle are observed throughout the region, which we interpret as the result of concentrations of fluids and silica enrichment derived from the subducted slab over millions of years. Low crustal average V_p/V_s ratios in the east and central Sea of Okhotsk indicate overall bulk felsic crustal composition. Generally, the crustal V_p/V_s ratios are higher than in the uppermost mantle; this is the result of higher Moho shear impedance contrasts than compressional impedance contrasts. Deep crustal enrichment in silica could also explain the moderately low V_p/V_s ratios in the crust. Efforts to constrain absolute seismic velocities and structure landward of the volcanic arc in other subduction zones are needed for assessing the generality of our findings.

[35] **Acknowledgments.** We thank Xiaobi Xie, Simon Peacock, Chuck Langston, and Peter Shearer for constructive comments. Quentin Williams and Jim Gill provided helpful suggestions on mantle petrology and the role of fluids. Digitized WWSSN data were provided by Zhi Zhang. Qiaoer Zhou helped with some text and figure editing work. This research was supported by NSF grant EAR0125595. This is contribution number 484 of the Center for the Study of Imaging and Dynamics of the Earth, IGPP, UCSC.

References

Aki, K., and P. G. Richards (1980), *Quantitative Seismology*, W. H. Freeman, New York.

Arai, S., Y. Shimizu, and F. Gervilla (2003), Quartz diorite veins in a peridotite xenolith from Tallante, Spain: Implications for reaction and survival of slab-derived SiO_2-oversaturated melt in the upper mantle, *Proc. Jpn. Acad., Ser. B*, *79*, 145–150.

Bebout, G. E., and M. D. Barton (1989), Fluid flow and metasomatism in a subduction zone hydrothermal system: Catalina Schist terrane, California, *Geology*, *17*, 976–980.

Birch, F. (1961), The velocity of compressional waves in rocks to 10 kilobars: 2, *J. Geophys. Res.*, *66*, 2199–2224.

Carbonell, R., W. P. Clement, and S. B. Smithson (1994), Joint P-wave and S-wave velocity determination from reflected PP, SS, and converted PS/SP phases from large-aperture seismic-reflection measurements, *Tectonophysics*, *232*, 379–389.

Chapman, M. E., and S. C. Solomon (1976), North American–Eurasian plate boundary in northeast Asia, *J. Geophys. Res.*, *81*, 921–930.

Christensen, N. I. (1996), Poisson's ratio and crustal seismology, *J. Geophys. Res.*, *101*, 3139–3156.

Christensen, N. I., and W. D. Mooney (1995), Seismic velocity structure and composition of the continental crust: A global view, *J. Geophys. Res.*, *100*, 9761–9788.

Cook, D. B., K. Fujita, C. A. McMullen, G. L. Johnson, and K. Kaminuma (1986), Present-day plate interactions in northeast Asia: North American, Eurasian, and Okhotsk plates, *J. Geodyn.*, *6*, 33–51.

DeMets, C. (1992), A test of present-day plate geometries for northeast Asia and Japan, *J. Geophys. Res.*, *97*, 17,627–17,635.

Dziewonski, A. M., and D. L. Anderson (1981), Preliminary reference Earth model (PREM), *Phys. Earth Planet. Inter.*, *25*, 297–356.

Fedotov, S. A., and L. B. Slavina (1968), An estimate of the longitudinal-wave velocities in the upper mantle under the northwestern part of the Pacific Ocean and Kamchatka, *Izv. Akad. Sci.*, *4*, 70–83.

Futterman, W. I. (1962), Dispersive body waves, *J. Geophys. Res.*, *67*, 5279–5291.

Gnibidenko, H. S., and I. I. Khvedchuk (1982), The tectonics of the Okhotsk Sea, *Mar. Geol.*, *50*, 155–198.

Gnibidenko, H. S., and A. Svarichevsky (1984), Tectonics of the South Okhotsk deep-sea basin, *Tectonophysics*, *102*, 225–244.

Gnibidenko, H. S., T. W. C. Hilde, and E. V. Gretskaya (1995), Kuril (South Okhotsk) backarc basin, in *Tectonics and Magmatism*, edited by B. Taylor, pp. 421–449, Springer, New York.

Haskell, N. A. (1953), The dispersion of surface waves on multilayered media, *Bull. Seismol. Soc. Am.*, *43*, 17–34.

Haskell, N. A. (1960), Crustal reflection of plane *SH* waves, *J. Geophys. Res.*, *65*, 4147–4150.

Ikeda, Y., R. J. Stern, H. Kagami, and C.-H. Sun (2000), Pb, Nd, and Sr isotopic constraints on the origin of Miocence basaltic rocks from northeast Hokkaido, Japan: Implications for the opening of the Kurile backarc basin, *Isl. Arc*, *9*, 161–172.

Jordan, T. H., and L. N. Frazer (1975), Crustal and upper mantle structure from *Sp* phases, *J. Geophys. Res.*, *80*, 1504–1518.

Katsumata, K., S. Tsukada, I. Ogino, and M. Mizoue (1993), Linear array data gathering for microearthquake observation: Survey of mid-crustal reflectors, *Geophys. Res. Lett.*, *20*, 411–414.

Kimura, G., and K. Tamaki (1986), Collision, rotation, and back-arc spreading in the region of the Okhotsk and Japan seas, *Tectonics*, *5*, 389–401.

Kimura, G., S. Miyashita, and S. Miyasaka (1983), Collision tectonics in Hokkaido and Sakhalin, in *Accretiona Tectonics in the Circum-Pacific Regions*, edited by M. Hashimoto and S. Uyeda, pp. 123–134, Terrapub, Tokyo.

Langston, C. A. (1979), Structure under Mount Rainier, Washington, inferred from teleseismic body waves, *J. Geophys. Res.*, *84*, 4749–4762.

Langston, C. A. (2001), The vertical component P-wave receiver function, *Bull. Seismol. Soc. Am.*, *91*, 1805–1819.

Lerner-Lam, A. L., and T. H. Jordan (1987), How thick are the continents?, *J. Geophys. Res.*, *92*, 14,007–14,026.

Levin, V., J. Park, J. Lees, M. T. Brandon, V. Peyton, E. Gordeev, and A. Ozerov (2002a), Crust and upper mantle of Kamchatka from teleseismic receiver functions, *Tectonophysics*, *358*, 233–265.

Levin, V., N. Shapiro, J. Park, and M. Ritzwoller (2002b), Seismic evidence for catastrophic slab loss beneath Kamchatka, *Nature*, *418*, 763–767.

Levshin, A. L., M. H. Ritzwoller, M. P. Barmin, A. Villasenor, and C. A. Padgett (2001), New constraints on the arctic crust and uppermost mantle: Surface wave group velocities, Pn and Sn, *Phys. Earth Planet. Inter.*, *123*, 185–204.

Maeda, J. (1990), Opening of the Kuril Basin deduced from the magmatic history of central Hokkaido, north Japan, *Tectonophysics*, *174*, 235–255.

Mooney, W. D., G. Laske, and T. G. Masters (1998), CRUST 5.1: A global crustal model at 5 degrees × 5 degrees, *J. Geophys. Res.*, *103*, 727–747.

Revenaugh, J., and T. H. Jordan (1989), A study of mantle layering beneath the western Pacific, *J. Geophys. Res.*, *94*, 5787–5813.

Riegel, S. A., K. Fujita, B. M. Koz'min, V. S. Imaev, and D. B. Cook (1993), Extrusion tectonics of the Okhotsk plate, northeast Asia, *Geophys. Res. Lett.*, *20*, 607–610.

Sato, H., and K. Ito (2002), Olivine-Pyroxene-H_2O system as a practical analogue for estimating the elastic properties of fluid-bearing mantle rocks at high pressures and temperatures, *Geophys. Res. Lett.*, *29*(9), 1325, doi:10.1029/2001GL014212.

Schenk, T., G. Muller, and W. Brustle (1989), Long-period precursors to *pP* from deep-focus earthquakes: The Moho underside reflection pMP, *Geophys. J. Int.*, *98*, 317–327.

Schwartz, S. Y., and T. Lay (1993), Complete PP waveform modeling for determining crust and upper mantle structure, *Geophys. J. Int.*, *112*, 210–224.

Seno, T., T. Sakurai, and S. Stein (1996), Can the Okhotsk plate be discriminated from the North American plate?, *J. Geophys. Res.*, *101*, 11,305–11,315.

Shapiro, N. M., and M. H. Ritzwoller (2002), Monte-Carlo inversion for a global shear-velocity model of the crust and upper mantle, *Geophys. J. Int.*, *151*, 88–105.

Takahashi, H., et al. (1999), Velocity field of around the Sea of Okhotsk and Sea of Japan regions determined from a new continuous GPS network data, *Geophys. Res. Lett.*, *26*, 2533–2536.

Takei, Y. (2002), Effect of pore geometry on V_P/V_S: From equilibrium geometry to crack, *J. Geophys. Res.*, *107*(B2), 2043, doi:10.1029/2001JB000522.

Ulmer, P., and V. Trommsdorff (1995), Serpentine stability to mantle depths and subduction-related magmatism, *Science*, *268*, 858–861.

Wagner, L. S., S. Beck, and G. Zandt (2005), Upper mantle structure in the south central Chilean subduction zone (30° to 36°S), *J. Geophys. Res.*, *110*, B01308, doi:10.1029/2004JB003238.

Watt, J. P., G. F. Davies, and R. J. O'Connell (1976), The elastic properties of composite materials, *Rev. Geophys.*, *14*, 541–563.

Wei, D., and T. Seno (1995), Determination of the Amurian Plate motion, *Eos Trans. AGU*, *76*(46), Fall Meet Suppl., F617.

Winter, J. D. (2001), *An Introduction to Igneous and Metamorphic Petrology*, Prentice-Hall, Upper Saddle River, N. J.

Worrall, D. M., V. Kruglyak, F. Kunst, and V. Kuznetsov (1996), Tertiary tectonics of the Sea of Okhotsk, Russia: Far-field effects of the India-Eurasia collision, *Tectonics*, *15*, 813–826.

Zandt, G., A. A. Velasco, and S. L. Beck (1994), Composition and thickness of the southern Altiplano crust, Bolivia, *Geology*, *22*, 1003–1006.

Zhang, Z., and T. Lay (1993), Investigation of upper mantle discontinuities near northwestern Pacific subduction zones using precursors to *sSH*, *J. Geophys. Res.*, *98*, 4389–4405.

Zhao, L. S., D. V. Helmberger, and D. G. Harkrider (1991), Shear-velocity structure of the crust and upper mantle beneath the Tibetan Plateau and southeastern China, *Geophys. J. Int.*, *105*, 713–730.

Zonenshain, L. P., and L. A. Savostin (1981), Geodynamics of the Baikal rift zone and plate tectonics of Asia, *Tectonophysics*, *76*, 1–45.

T. Lay and Y. Zheng, Earth Sciences Department, University of California, 1156 High Street, Santa Cruz, CA 95060, USA. (yzheng@es.ucsc.edu)